Article

A-Site Doping to Alter Oxygen Vacancy Diffusion in SrTiO$_3$

Gil M. Repa, Zachary J. Knepp, and Lisa A. Fredin*

Cite This: ACS Omega 2024, 9, 26719−26723

Read Online

ACCESS | Metrics & More | Article Recommendations | Supporting Information

ABSTRACT: Doped SrTiO$_3$ is a promising material for many applications where oxygen vacancy diffusion is either critical to device function or a source of failure. This work provides new insight into long-range oxygen vacancy diffusion in SrTiO$_3$ doped with Mn^{2+}, Cr^{3+}, or Fe^{2+} on the A-site. Density functional theory and the nudged elastic band method are used to calculate oxygen vacancy diffusion barriers adjacent to the dopant and at remote sites. Relative to the pure SrTiO$_3$ structure, doping was found to raise the diffusion barrier for V$_O^{\bullet\bullet}$ vacancies and lower the diffusion barrier for V$_O^x$ vacancies. Furthermore, a doping trapping radius of 6 Å was found for both the V$_O^x$ and V$_O^{\bullet\bullet}$ vacancies. Counterintuitively, trapping was observed even in supercells where vacancies and dopants are both positively charged. These results provide new insight into how less common A-site doping can change the electronic structure of this important material.
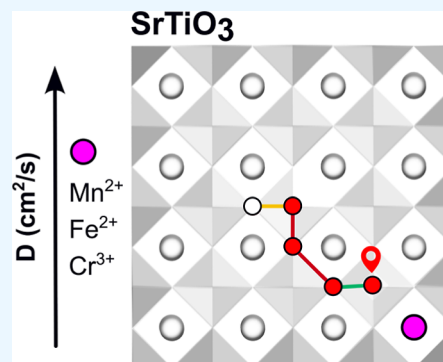
INTRODUCTION

The perovskite family of ceramic oxides represents some of the most widely used oxide materials today. Characterized by the chemical formula ABO$_3$ and comprising a network of corner-sharing BO$_6$ octahedra around A-site cations, perovskite oxides are targeted for the next generation of solid-state batteries,[1] fuel cells,[2] thermoelectrics,[3] photovoltaics,[4] and capacitors.[5] A large portion of this technological interest stems from the tolerance of the perovskite structure to accommodate a variety of different elements on each metal site, allowing high tunability through elemental composition[6] or doping.[4] As the archetypical perovskite oxide, SrTiO$_3$ serves as an ideal model system for understanding the properties of the larger family. Furthermore, SrTiO$_3$ has wide commercial use as a substrate for epitaxial growth and thus serves as the bottom electrode for many oxide thin-film electronic devices.[7] In other applications, the high dielectric constant of SrTiO$_3$ makes it a valuable material for transistors and capacitors,[5] and its electrical properties make it an appealing electrode for ionic conductors.[8]

The emergence of SrTiO$_3$ in a variety of device architectures has resulted in increased attention to defects of the crystal lattice, which often are the critical determinants of performance.[4] Arguably, the most important of these defects that arise during material processing are oxygen vacancies (V$_O$) and their subsequent long-range diffusion.[9] Indeed, this ionic diffusion may be the source of electronic device aging, giving rise to fatigue[10] and resistance degradation,[11] ultimately acting as a source of failure. Conversely, some applications actually seek to maximize the rate of diffusion of charged vacancies, as in energy fuel cells.[8] Therefore, significant research effort has been focused on understanding the distribution and kinetics of V$_O$ migration in perovskites under working conditions.

The migration path for V$_O$ diffusion is well established and involves an oxygen atom traveling along a TiO$_6$ octahedral edge[9] (Figure S1). Experimentally measured energetic barriers for this process in the pure material generally converge around 0.6 to 0.7 eV.[12−15] The ionic diffusion rate (D) can be altered by dopants,[16] such as Cr, Mn, and Fe. When doped on the B-site, these acceptor dopants are a source of oxygen vacancies during the synthetic process through the maintenance of charge neutrality.[17] Therefore, intentional doping can be seen as a design strategy to increase V$_O$, and such approaches have been utilized to improve the performance of fuel cells.[2] However, doping may also raise the activation energy (E$_a$) for V$_O$ diffusion. For example, in Ni-doped SrTiO$_3$, E$_a$ was measured to be ~1 eV, an increase of 0.4 eV from undoped SrTiO$_3$.[16] Electron paramagnetic resonance spectroscopy has also shown that V$_O$ trapping can occur through association with dopants.[15,18] Indeed, static lattice simulations of dopant-V$_O$ association in B-site acceptor-doped SrTiO$_3$ have shown that such events are complicated processes spanning several neighbor shells.[13] This dopant−vacancy association may represent an additional failure mechanism for electrodes[19] but may be useful to prevent oxidative degradation when SrTiO$_3$ is used as a coating.

The nature of V$_O$ diffusion in the presence of A-site dopants has largely been neglected. Although synthesis of A-site-doped materials does not directly create V$_O$ like B-site acceptor
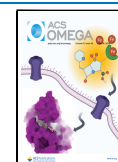
dopants, V_O is intrinsic in most synthesized oxide materials. Thus, the coexistence of A-site dopants with intrinsic defects like V_O in the same crystal is likely.[20] Indeed, A-site doping with transition metal ions, like Cr^{3+} and Mn^{2+}, has been confirmed experimentally on numerous occasions.[21−26] Additionally, lanthanide dopants on the A-site of $SrTiO_3$ anode materials have been shown to improve the performance of solid oxide fuel cells.[8] Therefore, a complete model of V_O diffusion in $SrTiO_3$ must provide a solid understanding of the effect of A-site dopants.

This study tackles the problem of V_O diffusion in A-site-doped $SrTiO_3$ by combining density functional theory (DFT) and the nudged elastic band (NEB) method to calculate the energetics of V_O migration in the presence of common A-site transition metal dopants Mn^{2+} (Mn_{Sr}^x) and Cr^{3+} (Cr_{Sr}') and a rare A-site dopant, Fe^{2+} (Fe_{Sr}^x). By utilizing large supercells, a comparable quantum-mechanical description along a multistep diffusion pathway is developed (Figure 1). The results show that the relative magnitude of E_a of V_O migration is highly dependent on the charge state of the defect, even at locations nonadjacent to the dopant. Furthermore, trapping of V_O at dopant sites is found to be a non-nearest-neighbor event with energetically favorable complexation spanning several neighbor shells.

■ COMPUTATIONAL METHODS

To obtain a quantum mechanical description of V_O diffusion in $SrTiO_3$, the electron projector-augmented wave (PAW) scheme of DFT, as implemented in the Vienna Ab initio Simulation Package (VASP),[27] was used. PBEsol,[28] a 600 eV cutoff for the plane-wave basis set, and pseudopotentials with core/valence configuration: Sr:[Ar]3d/4s4p5s, Ti:Ne/3s3p4s3d, O:He/2s2p, Cr:Ne 3s/3p4s3d, Mn:Ne/3s3p4s3d, and Fe:Ar/4s3d were used. All calculations were performed with spin polarization where each element was initialized in its high-spin configuration and an electronic convergence of 10^{-6} eV. Only the atom positions were relaxed, and calculations were carried out until the maximum force on any atom was less than 0.05 eV Å^{-1} in any direction. NEB calculations with 3 images along the path between the optimized initial and final V_O locations were carried out to calculate the E_a for each hop of the vacancy. Because of the high computational expense of performing calculations on such large unit cells, all calculations were performed at the Γ-point only.

PBEsol enabled the use of a large 325 atom 4 × 4 × 4 repeat of the primitive $SrTiO_3$ unit cell, allowing a direct quantum mechanical examination of V_O diffusion at distances far from the defect and at a defect concentration of approximately 10^{20} cm^{-3}. Previous calculations of V_O diffusion in $SrTiO_3$ have introduced the Hubbard U correction to account for the shortcomings of using a simple GGA functional to describe a highly correlated material.[29] To understand the ability of the PBEsol functional to reproduce the results of higher-level methods, calculated E_a was compared with single-point energies at the PBEsol-optimized geometries using a more accurate hybrid functional, HSEsol.[30] For 6 randomly selected transition states in a 3 × 3 × 3 $Mn_{Sr}^x-V_O^{\bullet\bullet}$ super cell, PBEsol predicted reasonable E_a values, with maximum deviation between the two methods at approximately 0.05 eV (Figure 2). This indicates that the relative energies predicted by PBEsol are reasonable.

Dopant structures were created by inserting the respective metal atom onto a Sr site, followed by optimization to a 5-
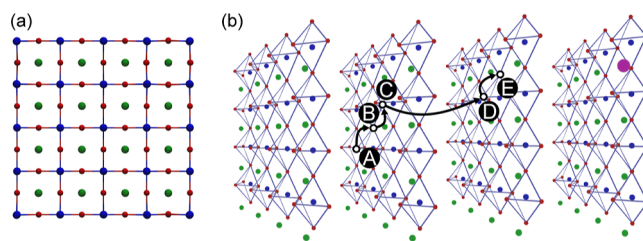
Figure 1. $SrTiO_3$ structure where the green, blue, red, and magenta spheres correspond to Sr, Ti, O, and dopant atoms, respectively. (a) Single layer in 2D and (b) simulated diffusion pathway for V_O in a four-layer perovskite crystal. Each site is labeled by the letters in black circles. V_O starts at the farthest possible site from the dopant (A) and diffuses directly toward the dopant, ending at the nearest possible nonbonding site (E).
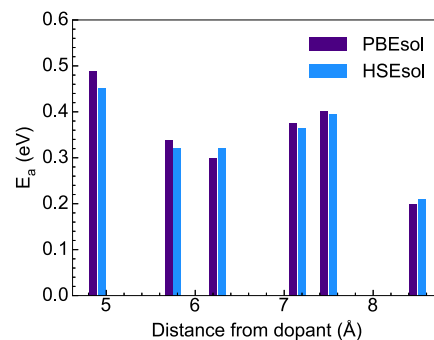

Figure 2. Comparison of PBEsol and HSEsol predicted E_a for $Mn_{Sr}^x-V_O^{\bullet\bullet}$ across 6 randomly selected hops in a 3 × 3 × 3 unit cell.

coordinate square pyramidal geometry that was previously shown to best reproduce the experimental hyperfine values for the A-site doping of Mn_{Sr}^x.[31] A V_O was then created and optimized at varying distances from the dopant to simulate a diffusion path in the crystal (Figure 1). The path was selected such that V_O began at the oxygen site furthest from the dopant (A), and over 3 intermediates (B,C,D) diffuses directly toward the dopant, terminating at one of the oxygens in the defected perovskite A-cell (but not bonded to the dopant, E). Both $V_O^{\bullet\bullet}$ (vacancy of O^{2-}) and V_O^x (vacancy of O^0) oxygen vacancies were examined, with the latter leading to 2 additional electrons in the supercell.

■ RESULTS AND DISCUSSION

The barrier for $V_O^{\bullet\bullet}$ migration in undoped $SrTiO_3$ supercells was approximately 0.2 eV. This slightly underestimates most previous experimental and theoretical results, reproducing similar values to those previously obtained using the same uncorrected GGA functional.[29] V_O^x-defected super cells predict a barrier of approximately 0.4 eV, which agrees with previous DFT results.[14] It is noted that deviation from the experimental value of 0.6−0.7 eV is expected from the under-localized charge density predicted by PBEsol. Previous studies of oxide materials have utilized the Hubbard U correction; however, the barrier is highly dependent on the chosen U value,[32] making it difficult to compare different dopants. The complex interplay of metal orbital energies, dopant electron density, ligand field, unpaired spins, and the resulting magnetic moments on Cr^{3+} and Mn^{2+} is multiconfigurational and highly correlated, which makes obtaining accurate energy levels of dopants in $SrTiO_3$ challenging for even the highest quality functionals available. Therefore, a careful analysis of any DFT
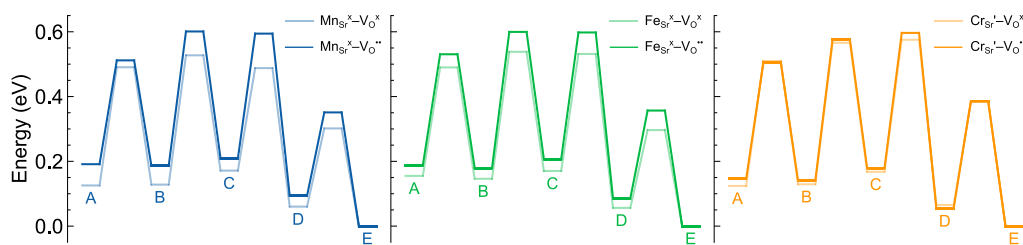
Figure 3. Energy profiles for $V_O^{\bullet\bullet}$ and V_O^x along the simulated diffusion path (Figure 1). V_O becomes associated with the dopant at D due to a large reversion barrier (TS_{DC}). Activation energies for the forward and reverse paths are plotted as bars in Figure 4.
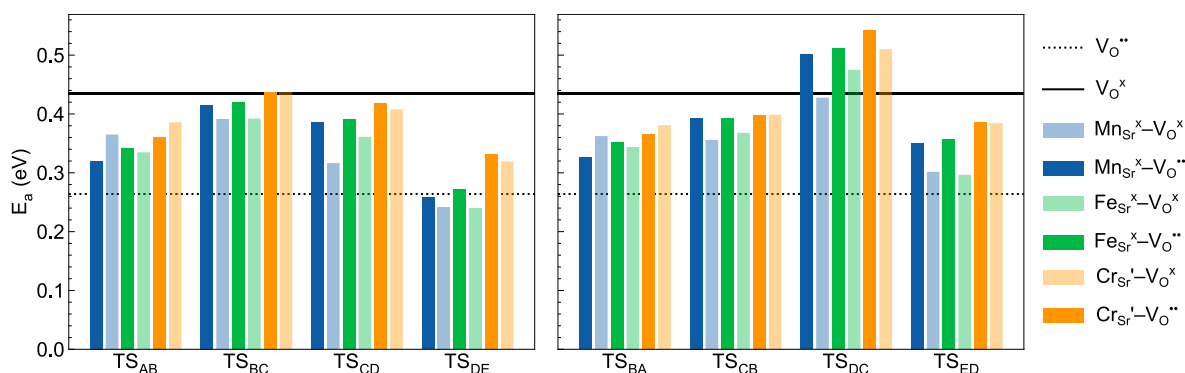
Figure 4. Activation energies (E_a) for the forward (left) and reverse (right) paths for $V_O^{\bullet\bullet}$ and V_O^x along the simulated diffusion path. $TS_{\alpha\beta}$ corresponds to the transition states from α to β geometries.

solution is required. In fact, even hybrid methods like HSE06 are unable to correctly predict the experimental spin state of Mn doped on the B-site,[31] limiting the current study to A-site dopants.

In all calculations, Bader analysis[33] revealed positive charges of +1.7, +1.4, and +1.4 for Cr^{3+}, Fe^{2+}, and Mn^{2+} dopants, respectively (Table S2). These values may only provide a partial picture of the electronic density around the dopant as meaningful charge assignment is dependent on factors like integration grid size[33] and choice of pseudopotential.[34] Furthermore, Bader and other charge partitioning schemes neglect effects such as polaron formation, which extends several neighbor shells around the dopant beyond the typical cutoff values. Previous first-principles calculations of the Cr_{Sr}' have indicated that the Cr 3d gap states appear near the bottom of the conduction band,[35] which have been a possible explanation for the visible-light absorption observed in experiment.[23] Transition levels for Mn_{Sr}^x defects have been found to occupy two midgap positions that were largely insensitive to the presence of a nearest neighbor V_O.[31] Here, calculations of the $Fe_{Sr}^x–V_O^x$ and $Fe_{Sr}^x–V_O^{\bullet\bullet}$ reveal a similar electronic structure to the previously reported $Mn_{Sr}^x–V_O$ defect with two nondegenerate occupied defect levels. Calculated formation energies[36] for each dopant and vacancy location (Figure S2) reveal that creation of all configurations is exothermic, with favorability generally increasing when the vacancy is nearer to the dopant.

For most V_O transition states studied here, doping with all elements raised the diffusion barrier relative to $V_O^{\bullet\bullet}$ diffusion and lowered relative to V_O^x diffusion in $SrTiO_3$ (Figure 4). In general, activation energy of the V_O hopping for the forward path, toward the dopant, ranged from ~0.24 to 0.44 eV (Table S1), with the largest barriers occurring at TS_{BC} for most dopants. Despite small differences in E_a at different points along the path, there were no geometric differences at any of

the transition states for all hops and dopants. Furthermore, each geometry well represents those previously calculated for the undoped structure using DFT and DFT + U methods.[29] Additional attempts were made to relate the magnitude of each E_a to structural parameters on the basis of Sr−Sr separation at the diffusion site, however, no correlation was found (Figure S3). Similar parameters have been previously suggested for descriptors of pure crystals.[37] The small differences in both migration E_a and total energy when V_O is far from the defect may be due to subtle long-range reconstructions of the unit cell.

The increased E_a for $V_O^{\bullet\bullet}$ in doped supercells can be justified by considering electrostatic repulsion between the positively charged $V_O^{\bullet\bullet}$ defect and the positively charged dopant ions. Interestingly, the reaction profiles indicate that both $V_O^{\bullet\bullet}$ and V_O^x are capable of dopant association regardless of the charge (Figure 3). Specifically, the energy stabilization of the vacancy-dopant-associated complex occurs at the second neighbor shell (at structure D) in all cells (Figure 3). The large barrier for migration away from the dopant (TS_{DC}) effectively traps the vacancy approximately 6 Å from the dopant. The dissociation barriers were 0.50, 0.51, and 0.54 eV for the $V_O^{\bullet\bullet}$ moving away from Mn^{2+}, Fe^{2+}, and Cr^{3+} dopants, respectively. The barriers for dissociation of V_O^x and the dopant are lower in energy, at 0.48, 0.43, and 0.51 eV for Fe^{2+}, Mn^{2+}, and Cr^{3+}, respectively.

Experimentally, oxygen vacancy dynamics are measured as bulk diffusion and reported as the diffusion constant (D). While the barriers clearly show that oxygen vacancy diffusion is not constant across the structure, insights may be gained by comparing the effect of each dopant on the overall diffusion in order to find the best dopants for either restricting or increasing vacancy migration. Experimental determinations of D for $SrTiO_3$ have been reported extensively.[12] Here, the average diffusion constant (D) over N hops for the forward

and reverse diffusion paths was calculated for each dopant using rates from the transition-state theory

$$D = \frac{1}{6N} \sum_{i}^{N} r^2 k_i \tag{1}$$

where r is the distance between adjacent O atoms in the pure crystal structure, and k is the rate of the reaction determined from the calculated E_a via the Eyring equation

$$k_i = \frac{k_B T}{h} \exp\left(-\frac{E_{a,i}}{k_B T}\right) \tag{2}$$

where h is Planck's constant, k_B is Boltzmann's constant, and T is the temperature. Here, we report D at $T = 1000$ K as it is commonly reported in experimental measurements of V_O diffusion. If neglecting the effects of dopant trapping, linear scaling between temperatures is expected.

D for $V_O^{\bullet\bullet}$ systems is reduced vs the pure structure, as shown in Table 1. Specifically, average diffusivity decreases

Table 1. Average Activation Energies ($\overline{E}_a$) and Diffusion Constants (D) at 1000 K for $V_O^{\bullet\bullet}$ and $V_O^{x a}$

defect	$\overline{E}_a$/eV	D/cm^2 s^{-1} [1000 K]
V_O^x	0.43	1.10×10^{-4}
$V_O^{\bullet\bullet}$	0.26	7.94×10^{-4}
$Mn_{Sr}^x - V_O^x$	0.35 (0.05)	3.81×10^{-4}
$Mn_{Sr}^x - V_O^{\bullet\bullet}$	0.37 (0.07)	3.12×10^{-4}
$Fe_{Sr}^x - V_O^x$	0.35 (0.06)	3.74×10^{-4}
$Fe_{Sr}^x - V_O^{\bullet\bullet}$	0.38 (0.07)	2.67×10^{-4}
$Cr_{Sr}' - V_O^x$	0.40 (0.05)	1.85×10^{-4}
$Cr_{Sr}' - V_O^{\bullet\bullet}$	0.40 (0.06)	1.87×10^{-4}

^{a}Standard deviations are in parentheses.

$V_O^{\bullet\bullet} > Mn_{Sr}^x - V_O^x > Fe_{Sr}^x - V_O^x > Mn_{Sr}^x - V_O^{\bullet\bullet} > Fe_{Sr}^x - V_O^{\bullet\bullet} > Cr_{Sr}' - V_O^{\bullet\bullet} > Cr_{Sr}' - V_O^x > V_O^x$. This represents a range of D of almost an order of magnitude at 1000 K. It is critical to note that this approach to calculate D neglects effects like the ionic trapping as discussed above, which would require considerably more advanced analytical models[13] or possibly kinetic Monte Carlo techniques. Development of such models that can reliably calculate the effect of doping on measurable properties should be a priority for future studies.

CONCLUSIONS

Overall, this study provides quantum mechanical insights into V_O diffusion in A-site-doped SrTiO$_3$. The results indicate that dopants either raise or lower the barriers of V_O diffusion depending on the charge of the vacancy. V_O trapping through dopant association was observed even for dopants and vacancies with the same charge. Furthermore, the radius of V_O trapping is not dependent on the charge of the vacancy or the charge of the dopant. Such insights represent the first quantum mechanical picture of V_O diffusion in A-site-doped SrTiO$_3$ and will be critical in developing design criteria to targeted diffusion characteristics in SrTiO$_3$ through doping.

ASSOCIATED CONTENT

Supporting Information

The Supporting Information is available free of charge at https://pubs.acs.org/doi/10.1021/acsomega.4c04099.

SrTiO$_3$ structure and V_O diffusion pathway, all diffusion barriers, formal charges on the dopant, formation energies for each dopant and vacancy configuration, and correlation between E$_a$ for V_O diffusion and the separation of two nearest neighbor Sr atoms (PDF)

AUTHOR INFORMATION

Corresponding Author

Lisa A. Fredin − Department of Chemistry, Lehigh University, Bethlehem, Pennsylvania 18015, United States; orcid.org/0000-0002-4091-0899; Email: lafredin@lehigh.edu

Authors

Gil M. Repa − Department of Chemistry, Lehigh University, Bethlehem, Pennsylvania 18015, United States

Zachary J. Knepp − Department of Chemistry, Lehigh University, Bethlehem, Pennsylvania 18015, United States

Complete contact information is available at:
https://pubs.acs.org/10.1021/acsomega.4c04099

Notes

The authors declare no competing financial interest.

REFERENCES

(1) Tan, P.; Liu, M.; Shao, Z.; Ni, M. Recent Advances in Perovskite Oxides as Electrode Materials for Nonaqueous Lithium−Oxygen Batteries. Adv. Energy Mater. 2017, 7, 1602674.

(2) Shah, M. A. K. Y.; Rauf, S.; Zhu, B.; Mushtaq, N.; Yousaf, M.; Lund, P. D.; Xia, C.; Asghar, M. I. Semiconductor Nb-Doped SrTiO$_3$ Perovskite Electrolyte for a Ceramic Fuel Cell. ACS Appl. Energy Mater. 2021, 4, 365−375.

(3) Haque, M. A.; Kee, S.; Villalva, D. R.; Ong, W.; Baran, D. Halide Perovskites: Thermal Transport and Prospects for Thermoelectricity. Adv. Sci. 2020, 7, 1903389.

(4) Xu, Y.; Liang, Y.; He, Q.; Xu, R.; Chen, D.; Xu, X.; Hu, H. Review of doping SrTiO3 for photocatalytic applications. Bull. Mater. Sci. 2022, 46, 6.

(5) Hou, C.; Huang, W.; Zhao, W.; Zhang, D.; Yin, Y.; Li, X. Ultrahigh Energy Density in SrTiO$_3$ Film Capacitors. ACS Appl. Mater. Interfaces 2017, 9, 20484−20490.

(6) Pazik, R.; Seisenbaeva, G. A.; Wiglusz, R. J.; Kepinski, L.; Kessler, V. G. Crystal Structure and Morphology Evolution in the LaXO$_3$, X = Al, Ga, In Nano-Oxide Series. Consequences for the Synthesis of Luminescent Phosphors. Inorg. Chem. 2011, 50, 2966−2974.

(7) Pai, Y.-Y.; Tylan-Tyler, A.; Irvin, P.; Levy, J. Physics of SrTiO$_3$-based heterostructures and nanostructures: a review. Rep. Prog. Phys. 2018, 81, 036503.

(8) Li, R.; Zhang, C.; Liu, J.; Zhou, J.; Xu, L. A review on the electrical properties of doped SrTiO$_3$ as anode materials for solid oxide fuel cells. Mater. Res. Express 2019, 6, 102006.

(9) De Souza, R. A. Oxygen Diffusion in SrTiO$_3$ and Related Perovskite Oxides. Adv. Funct. Mater. 2015, 25, 6326−6342.

(10) Dawber, M.; Scott, J. F. A model for fatigue in ferroelectric perovskite thin films. Appl. Phys. Lett. 2000, 76, 1060−1062.

(11) Liu, W.; Randall, C. A. Thermally Stimulated Relaxation in Fe-Doped SrTiO$_3$ Systems: II. Degradation of SrTiO$_3$ Dielectrics. *J. Am. Ceram. Soc.* **2008**, *91*, 3251−3257.

(12) De Souza, R. A.; Metlenko, V.; Park, D.; Weirich, T. E. Behavior of oxygen vacancies in single-crystal SrTiO 3: Equilibrium distribution and diffusion kinetics. *Phys. Rev. B: Condens. Matter Mater. Phys.* **2012**, *85*, 174109.

(13) Schie, M.; Waser, R.; De Souza, R. A. A Simulation Study of Oxygen-Vacancy Behavior in Strontium Titanate: Beyond Nearest-Neighbor Interactions. *J. Phys. Chem. C* **2014**, *118*, 15185−15192.

(14) Carrasco, J.; Illas, F.; Lopez, N.; Kotomin, E. A.; Zhukovskii, Y. F.; Evarestov, R. A.; Mastrikov, Y. A.; Piskunov, S.; Maier, J. First-principles calculations of the atomic and electronic structure of F centers in the bulk and on the (001) surface of Sr Ti O 3. *Phys. Rev. B: Condens. Matter Mater. Phys.* **2006**, *73*, 064106.

(15) Müller, K. Paramagnetic point and pair defects in oxide perovskites. *J. Phys.* **1981**, *42*, 551−557.

(16) Waser, R. Bulk Conductivity and Defect Chemistry of Acceptor-Doped Strontium Titanate in the Quenched State. *J. Am. Ceram. Soc.* **1991**, *74*, 1934−1940.

(17) Merkle, R.; Maier, J. How Is Oxygen Incorporated into Oxides? A Comprehensive Kinetic Study of a Simple Solid-State Reaction with SrTiO $_3$ as a Model Material. *Angew. Chem., Int. Ed.* **2008**, *47*, 3874−3894.

(18) Merkle, R.; Maier, J. Defect association in acceptor-doped SrTiO $_3$: case study for FeTiVO and MnTiVO. *Phys. Chem. Chem. Phys.* **2003**, *5*, 2297−2303.

(19) Ascienzo, D.; Kurt, O.; Greenbaum, S.; Bayer, T. J. M.; Russell, M.; Wang, J.; Randall, C. A.; Ren, Y. Local structural changes due to the electric field-induced migration of oxygen vacancies at Fe-doped SrTiO $_3$ interfaces. *J. Am. Ceram. Soc.* **2019**, *102*, 4353−4366.

(20) Fu, Q.-Q.; Gu, H.; Xing, J.-J.; Cao, Z.; Wang, J. Controlling the A-site deficiency and oxygen vacancies by donor-doping in pre-reductive-sintered thermoelectric SrTiO3 ceramics. *Acta Mater.* **2022**, *229*, 117785.

(21) Levin, I.; Krayzman, V.; Woicik, J.; Tkach, A.; Vilarinho, P. X-ray absorption fine structure studies of Mn coordination in doped perovskite SrTiO3. *Appl. Phys. Lett.* **2010**, *96*, 052904.

(22) Maier, R. A.; Cockayne, E.; Donohue, M.; Cibin, G.; Levin, I. Substitutional Mechanisms and Structural Relaxations for Manganese in SrTiO $_3$: Bridging the Concentration Gap for Point-Defect Metrology. *Chem. Mater.* **2020**, *32*, 4651−4662.

(23) Bi, Y.; Ehsan, M. F.; Huang, Y.; Jin, J.; He, T. Synthesis of Cr-doped SrTiO3 photocatalyst and its application in visible-light-driven transformation of CO2 into CH4. *J. CO2 Util.* **2015**, *12*, 43−48.

(24) Yu, H.; Ouyang, S.; Yan, S.; Li, Z.; Yu, T.; Zou, Z. Sol−gel hydrothermal synthesis of visible-light-driven Cr-doped SrTiO3 for efficient hydrogen production. *J. Mater. Chem.* **2011**, *21*, 11347.

(25) Jiao, Z.; Chen, T.; Xiong, J.; Wang, T.; Lu, G.; Ye, J.; Bi, Y. Visible-light-driven photoelectrochemical and photocatalytic performances of Cr-doped SrTiO3/TiO2 heterostructured nanotube arrays. *Sci. Rep.* **2013**, *3*, 2720.

(26) Wang, D.; Ye, J.; Kako, T.; Kimura, T. Photophysical and Photocatalytic Properties of SrTiO $_3$ Doped with Cr Cations on Different Sites. *J. Phys. Chem. B* **2006**, *110*, 15824−15830.

(27) Kresse, G.; Furthmüller, J. Efficient iterative schemes for *ab initio* total-energy calculations using a plane-wave basis set. *Phys. Rev. B: Condens. Matter Mater. Phys.* **1996**, *54*, 11169−11186.

(28) Perdew, J. P.; Ruzsinszky, A.; Csonka, G. I.; Vydrov, O. A.; Scuseria, G. E.; Constantin, L. A.; Zhou, X.; Burke, K. Restoring the Density-Gradient Expansion for Exchange in Solids and Surfaces. *Phys. Rev. Lett.* **2008**, *100*, 136406.

(29) Zhang, L.; Liu, B.; Zhuang, H.; Kent, P.; Cooper, V. R.; Ganesh, P.; Xu, H. Oxygen vacancy diffusion in bulk SrTiO3 from density functional theory calculations. *Comput. Mater. Sci.* **2016**, *118*, 309−315.

(30) Heyd, J.; Scuseria, G. E.; Ernzerhof, M. Hybrid functionals based on a screened Coulomb potential. *J. Chem. Phys.* **2003**, *118*, 8207−8215.

(31) Repa, G. M.; Fredin, L. A. Mn environment in doped SrTiO3 revealed by first-principles calculation of hyperfine splittings. *Appl. Phys. Lett.* **2022**, *121*, 022401.

(32) Brown, J. J.; Page, A. J. Reaction pathways in the solid state and the Hubbard U correction. *J. Chem. Phys.* **2021**, *154*, 124121.

(33) Tang, W.; Sanville, E.; Henkelman, G. A grid-based Bader analysis algorithm without lattice bias. *J. Phys.: Condens. Matter* **2009**, *21*, 084204.

(34) Henkelman, G.; Arnaldsson, A.; Jónsson, H. A fast and robust algorithm for Bader decomposition of charge density. *Comput. Mater. Sci.* **2006**, *36*, 354−360.

(35) Wei, W.; Dai, Y.; Jin, H.; Huang, B. Density functional characterization of the electronic structure and optical properties of Cr-doped SrTiO $_3$. *J. Phys. D: Appl. Phys.* **2009**, *42*, 055401.

(36) Repa, G. M.; Fredin, L. A. Parameter space exploration reveals interesting Mn-doped SrTiO $_3$ structures. *Phys. Chem. Chem. Phys.* **2021**, *23*, 23486−23500.

(37) Kilner, J.; Brook, R. A study of oxygen ion conductivity in doped non-stoichiometric oxides. *Solid State Ionics* **1982**, *6*, 237−252.

(38) Towns, J.; Cockerill, T.; Dahan, M.; Foster, I.; Gaither, K.; Grimshaw, A.; Hazlewood, V.; Lathrop, S.; Lifka, D.; Peterson, G. D.; Roskies, R.; Scott, J. R.; Wilkins-Diehr, N. XSEDE: Accelerating Scientific Discovery. *Comput. Sci. Eng.* **2014**, *16*, 62−74.